



InterOptimus: An AI-assisted robust workflow for screening ground-state heterogeneous interface structures in lithium batteries[☆]

Yaoshu Xie^a, Jun Yang^a, Yun Cao^a, Wei Lv^a, Yan-Bing He^a, Lu Jiang^{b,*}, Tingzheng Hou^{a,*}

^a Institute of Materials Research (iMR), Tsinghua Shenzhen International Graduate School, Tsinghua University, Shenzhen 518055, Guangdong, China

^b City University of Hong Kong (Dongguan), Dongguan 523808, Guangdong, China

ARTICLE INFO

Article history:

Received 18 February 2025

Revised 28 February 2025

Accepted 2 March 2025

Available online 20 March 2025

Keywords:

Heterogeneous interfaces

Lithium batteries

Machine learning interatomic potentials

Lattice matching

Interface energy

ABSTRACT

The formation of interphase layers, including the cathode-electrolyte interphase (CEI) and solid-electrolyte interphase (SEI), exhibits significant chemical complexity and plays a pivotal role in determining the performance of lithium batteries. Despite considerable advances in simulating the bulk phase properties of battery materials, the understanding of interfaces, including crystalline interfaces that represent the simplest case, remains limited. This is primarily due to challenges in performing ground-state searches for interface microstructures and the high computational costs associated with first-principles methods. Herein, we introduce InterOptimus, an automated workflow designed to efficiently search for ground-state heterogeneous interfaces. InterOptimus incorporates a rigorous, symmetry-aware equivalence analysis for lattice matching and termination scanning. Additionally, it introduces stereographic projection as an intuitive and comprehensive framework for visualizing and classifying interface structures. By integrating universal machine learning interatomic potentials (MLIPs), InterOptimus enables rapid predictions of interface energy and stability, significantly reducing the necessary computational cost in density functional theory (DFT) by over 90%. We benchmarked several MLIPs at three critical lithium battery interfaces, $\text{Li}_2\text{S}/\text{Ni}_3\text{S}_2$, LiF/NCM , and $\text{Li}_3\text{PS}_4/\text{Li}$, and demonstrated that the MLIPs achieve accuracy comparable to DFT in modeling potential energy surfaces and ranking interface stabilities. Thus, InterOptimus facilitates the efficient determination of ground-state heterogeneous interface structures and subsequent studies of structure-property relationships, accelerating the interface engineering of novel battery materials.

© 2025 Science Press and Dalian Institute of Chemical Physics, Chinese Academy of Sciences. Published by Elsevier B.V. and Science Press. All rights are reserved, including those for text and data mining, AI training, and similar technologies.

1. Introduction

The increasing demand for electric vehicles and portable electronic devices necessitates the development of next-generation batteries with high reversible capacity, exceptional stability, and reduced cost. Most battery systems integrate multiple components, such as active materials, solid electrolytes, and conductive additives, resulting in inherently complex interfacial contacts and reconstructions [1–4]. Optimizing battery performance thus requires the precise control of interfacial chemistry, particularly for high-energy batteries that incorporate high-capacity lithium

metal anodes and high-voltage cathodes [5–10]. In many cases, electrolytes with limited electrochemical stability windows can be deliberately allowed to react with either the high-voltage cathode or low-voltage anode during the initial charge-discharge cycles. The reaction cascades can lead to the formation of a stable, passivated cathode-electrolyte interphase (CEI) or anode solid-electrolyte interphase (SEI), provided the interphase exhibits sufficiently high ionic conductivity and low electronic conductivity [3,11]. This principle applies across various electrolyte systems, whether solid or liquid, inorganic or organic, thereby broadening the range of viable materials choices. The formation of heterogeneous interfaces creates distinct chemical environments, which significantly influence key electrochemical and physical processes governing battery performance [3,12]. Moreover, the interphase layers are believed to comprise multiple chemical compounds that differ from the bulk regions [1,13–15], further complicating interfacial electrochemical behaviors. Despite their critical role, the

[☆] This article is part of a special issue entitled: ‘AI4Batteries’ published in Journal of Energy Chemistry.

* Corresponding authors.

E-mail addresses: lu.jiang@cityu-dg.edu.cn (L. Jiang), tingzhenghou@sz.tsinghua.edu.cn (T. Hou).

structure-property relationships of these heterogeneous interfaces remain poorly understood. Advancing the understanding of the structure and property of the interface region is crucial for optimizing material selection and fabrication strategies for next-generation lithium batteries.

Computational studies have provided valuable insights into the bulk phase properties of crystalline cathode, anode, and electrolyte materials, including thermodynamic stability, electrochemical stability window, ion conductivity, and electronic structures. These advancements have been largely driven by explicit atomistic simulations of well-defined crystalline structures [16–22]. Most recently, this research area has been further advanced by the surge in artificial intelligence (AI) and its predictive and generative applications in materials science [23–29]. Despite the extensive theoretical studies on the bulk-phase properties, research on the interface properties remains significantly limited, even for the simplest cases involving crystalline interfaces. To theoretically investigate the property of a specific interface, one can apply an explicit or implicit approach, depending on whether an interface comprising two distinctive crystals is utilized in the simulation model. Most studies rely on implicit approaches, which extrapolate interface properties from the calculated bulk phase or slab phase properties [22], or explicit approaches that focus on a restricted and non-exhaustive set of materials and interface structures [20]. The challenge of scaling up explicit interface modeling and simulations has notably hindered the development of high-quality crystalline interface databases. Specifically, the primary difficulty in modeling explicit crystalline interfaces lies in the complex structural and geometric optimization of interface bicrystal model (IBM) [30,31], due to theoretically infinite possible variants of interfacial lattice plane orientation, termination, relative position between two half-crystals, and potential atomic rearrangements. IBM is

constructed by combining two coherent slabs under periodic boundary conditions. However, it should be noted that, in practice, the two distinctive slabs are typically incoherent. As a result, a relatively small strain is generally required to enforce a coherent lattice match between the slabs in the IBM of heterogeneous interface. The process of searching for such coherent possibilities is termed as two-dimensional (2D) lattice matching. Fig. 1 illustrates the process of generating an optimized IBM. Prior to atomic relaxation, a vast number of interface structure variants can be generated through iterative exploration and sampling processes, including lattice matching, termination selection, and rigid body translation. Therefore, the key challenges in traditional interface simulations stem from the labor-intensive manual procedures and the high computational cost of first-principles calculations required to explore the energy landscape of all possible interface structures.

In this work, we introduce InterOptimus, an automated workflow designed to address key challenges in atomic simulations of heterogeneous interfaces. This workflow implements more robust symmetry analysis algorithms by considering symmetrically equivalent relationships in the IBM framework. Compared with existing tools [32–34], this method significantly reduces the likelihood of overlooking non-equivalent interfaces. It also employs stereographic projection to explicitly present all lattice matching possibilities, which aligns with crystallographic conventions and is more widely accepted. This tool is more efficient to visualize all the possibilities of two arbitrary crystals to form stable interfaces including the distribution of equivalent and non-equivalent lattice matches, which more intuitively illustrates the anisotropy of interface formation preference in a three-dimensional framework. Additionally, it integrates state-of-the-art universal machine learning interatomic potentials (MLIPs) to accelerate the explo-

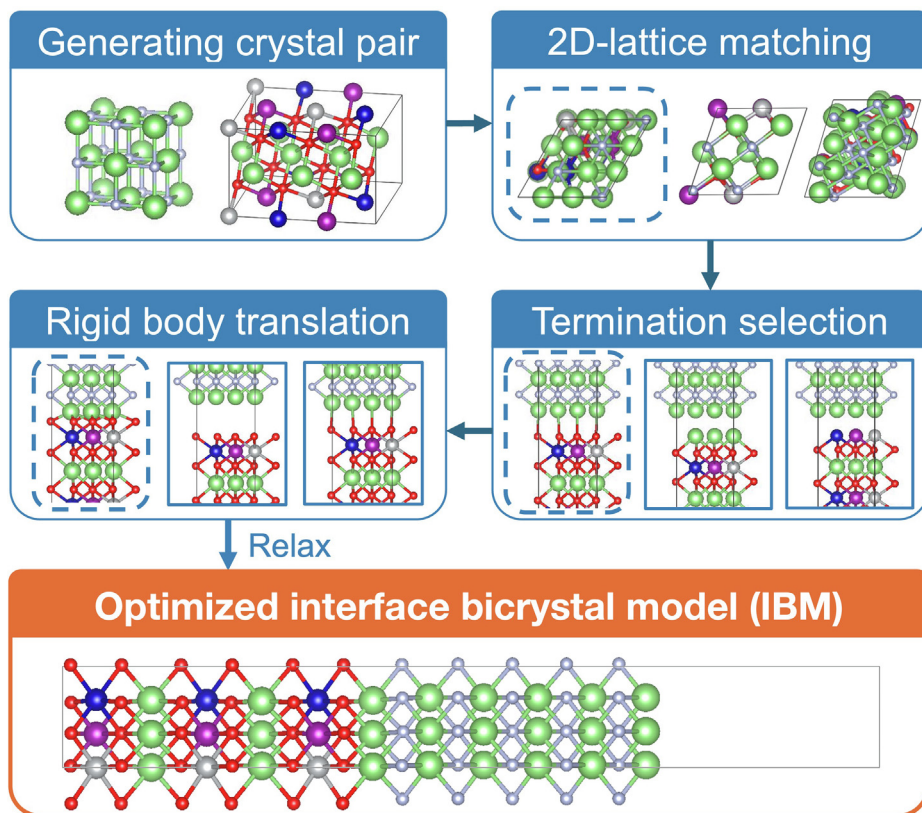


Fig. 1. Steps to optimize a coherent heterogeneous interface.

ration of ground-state interface structures with the combination of good efficiency and decent accuracy, with tests validation in interface systems including the non-reactive $\text{Li}_2\text{S}|\text{Ni}_3\text{S}_2$ and $\text{LiF}|\text{NCM}$, and the reactive $\text{Li}_3\text{PS}_4|\text{Li}$. Specifically, the interface energy ranking results illustrate that a selected universal MLIP ORB [35] with a notably low computational cost (around 4.44 in central processing unit (CPU) core seconds per relaxation step for a 118-atom system) successfully identified the ground-state interface structures for all of the three interface systems with an efficiency promotion over 90%, achieving an effective interface energy accuracy within 0.30 J m^{-2} and with ranking robustness reflected by Spearman's rank correlation coefficient reaching 0.90. Our method provides a powerful and computationally efficient tool for atomic-level investigations into crystalline interfaces, applicable to systems including CEIs and SEIs in batteries. It holds great promise for advancing next-generation high-performance batteries by providing important theoretical insights into structural design and materials selection to form beneficial interphases.

2. Methods

Fig. 2 illustrates the workflow of InterOptimus, which consists of three iterative layers: lattice matching, termination scanning, and rigid body translation (RBT) & Pre-DFT-optimization. The iterative process begins with two arbitrary crystals. Firstly, it searches for all the possible coherent lattice matches within allowed strain and matching area. Each explored lattice match i_m specifies two lattice planes which are utilized as the basal planes to make two slabs to be combined to form the interface. Then, each of the two basal planes can choose different atomic planes to expose the slab surfaces to be combined for interface construction, termed as the termination of the interface. Finally, we label the selected lattice match i_m and termination i_t as a (i_m, i_t) group. Each group includes disparate interface structures constructed by performing RBT of one slab respect to the other before atomic relaxation. Therefore, the process to find the ground-state interface constructed by two arbitrary crystals is divided into two steps: (1) exhaustively searching for all the non-equivalent lattice matches and terminations to specify all the possible non-equivalent (i_m, i_t) groups; (2) for each (i_m, i_t) group, finding the optimal RBT and the corresponding relaxed lowest-energy interface.

2.1. Lattice matching

Lattice matching is performed using the SubstrateAnalyzer class in Pymatgen [33], which employs the Zur & McGill algorithm [36] to identify two-dimensional lattice matches between arbitrary crystal pairs. This method treats the two crystals as a film and a substrate, applying strain necessary for lattice matching solely to the film. A lattice match consists of two 2D lattices, where the film basis $[\nu_{f1}, \nu_{f2}]$ being coherent with the substrate basis $[\nu_{s1}, \nu_{s2}]$. Given two obtained lattice matches, match A and match B, denoted as $[\nu_{f1}^A, \nu_{f2}^A]||[\nu_{s1}^A, \nu_{s2}^A]$ and $[\nu_{f1}^B, \nu_{f2}^B]||[\nu_{s1}^B, \nu_{s2}^B]$, the two film bases $[\nu_{f1}^A, \nu_{f2}^A]$, $[\nu_{f1}^B, \nu_{f2}^B]$, or the substrate bases $[\nu_{s1}^A, \nu_{s2}^A]$, $[\nu_{s1}^B, \nu_{s2}^B]$, can be regarded as equivalent if they are related by a symmetry operation of the film/substrate crystal group or a superlattice transformation. If both the film and substrate bases of A and B are equivalent, the two matches are identified as equivalent matches. Fig. S1 illustrates the detailed algorithm used to determine lattice match equivalence, which we employed to extract all non-identical matches presented in this work. This algorithm then groups the matching results based on equivalence, and selects the match with the smallest matching area in each group for subsequent calculations.

2.2. Termination scanning

For a given lattice match, different interfaces can be formed by combining distinct atomic or motif plane terminations of the film and substrate. To exhaustively generate these interfaces while preserving stereochemistry, we scan along the periodic boundary condition normal to the lattice plane (Fig. 2), resulting in distinct sets of film and substrate slabs. The complete set of possible terminations is obtained as the Cartesian product of these slab sets. We note that all IBMs in this study incorporate a vacuum region. To determine the equivalence of two arbitrary terminations while considering this vacuum, we developed an equivalence detection algorithm, which comprehensively analyzed symmetries of the two component slabs and those relating them, as illustrated in Fig. S2(a). Existing approaches in Pymatgen [33] and Ogré [32,34] assess this equivalence based only on isolated film and substrate slabs, which does not guarantee equivalence for bicrystal terminations unless their structural transformations align with changes in

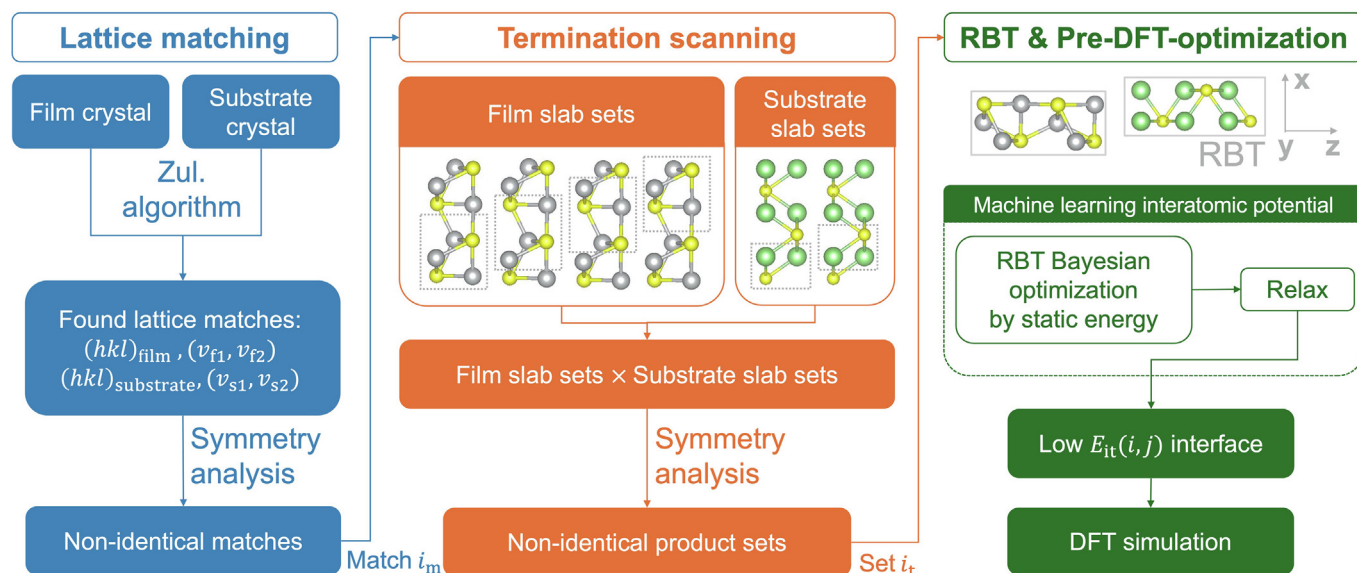


Fig. 2. InterOptimus framework.

the film-substrate disorientation and plane normal orientation. Fig. S2(b) illustrates an intuitive example presenting that equivalent isolated slabs can result in very disparate interface structures.

2.3. Rigid body translation (RBT)

Due to the complex potential energy surface (PES) of an interface system, different initial RBT configurations may relax into distinct final IBMs with varying interface energies. Therefore, optimizing the RBT is crucial for identifying the global energy minimum [37]. As shown in Fig. 2, specifying a lattice match i_m and a termination i_t , denoted as (i_m, i_t) , one can generate a group of disparate interfaces by relaxing IBMs with differently sampled RBT vector. In this work, we approximate the optimal RBT by using the non-relaxed energy as a proxy, assuming that a lower non-relaxed energy correlates with a lower relaxed energy. Then, the interface with optimized RBT will be subsequently relaxed as the most stable interface of (i_m, i_t) , denoted as $I(i_m, i_t)$. This static evaluation method, also known as γ -surface method, has been successfully applied in previous first-principles studies on grain boundary optimization [37]. Despite the assumption, frequent sampling interface energies in the RBT space using density functional theory (DFT) remains computationally expensive. To enhance efficiency, we employ Bayesian optimization with universal MLIPs to predict the static energy inspired by previous studies [32,34,38]. To further improve computational efficiency, we constrain the sampling space to the cell of non-identical displacement (CNID) [39,40], as calculated using the interface_master package [41]. CNID represents the minimum unit cell that includes all unique displacement patterns of two coherent, overlapping 2D lattices. In contrast, previous studies have typically sampled RBT points within the 2D coincident site lattice (CSL) [42,43], which is equal or larger than CNID, leading to redundant computations due to duplicate structure sampling [44]. Through the workflow design, InterOptimus minimizes computational overhead into only one to several runs of DFT structure optimizations while maintaining accuracy in interface optimization.

2.4. Validation for universal MLIPs

We evaluated the performance of several pre-trained universal MLIPs, including CHGNet [45], eqV2 [46], ORB [35], SevenNet [47], GRACE-2L [48], and MACE [49]. While Bayesian optimization is efficient for RBT optimization, it exhibits bias in sampling the PES. An unbiased sampling in PES is important to evaluate the robustness of MLIPs in PES description. Therefore, for each lattice match and termination group (i_m, i_t) , we randomly sampled 50 RBT points and computed the static IBM supercell energy E_{ht} , effective interface energy E_{it} (as proposed by Toso et al. [34]), and cohesive energy E_{ch} using both MLIPs and DFT. The definition of E_{it} and E_{ch} is as follows

$$E_{it} = \frac{E_{ht} - \frac{1}{2} (E_{slab,2}^{film} + E_{slab,2}^{substrate})}{A} \quad (1)$$

$$E_{ch} = \frac{E_{ht} - (E_{slab,1}^{film} + E_{slab,1}^{substrate})}{A} \quad (2)$$

where E_{ht} , $E_{slab,2}^{film}$, $E_{slab,2}^{substrate}$, $E_{slab,1}^{film}$, and $E_{slab,1}^{substrate}$ are illustrated in Fig. 3. The parameter A represents the interface area in the bicrystal model. Additionally, f_i and s_j denote the surface energies per unit area of the i -th and j -th surfaces in the film and substrate slabs, respectively. The bulk energies of the film and substrate are represented by E_{bulk}^{film} and $E_{bulk}^{substrate}$. The true interface energy γ represents the excess energy due to the existence of an interface. However, cal-

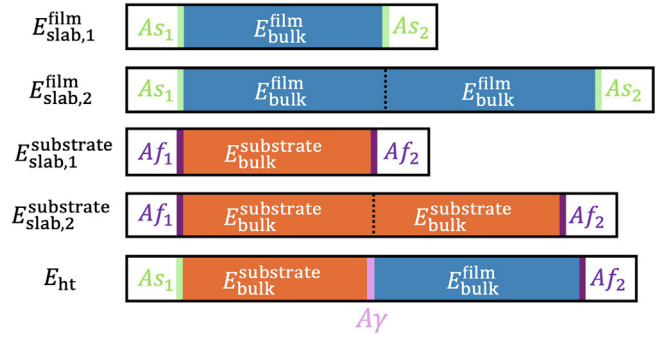


Fig. 3. Schematics of the supercells and corresponding energy compositions to calculate cohesive energy and effective interface energy.

culating γ is particularly challenging when the film or substrate slabs have two non-identical surfaces [50], which is common in ionic compounds. Traditionally, interface stability has been assessed using cohesive energy E_{ch} , but this metric depends on the two surface energies f_1 and s_2 (Fig. 3), making it unreliable for comparing relative stabilities. To address this issue, Toso et al. [34] introduced the concept of effective interface energy E_{it} , which better captures the thermodynamic tendency of an interface to disrupt domain growth and switch to another phase. The relationship between E_{it} and the true excess interface energy γ can be derived as follows.

$$E_{slab,1}^{film} = E_{bulk}^{film} + Af_1 + Af_2 \quad (3)$$

$$E_{slab,2}^{film} = 2E_{bulk}^{film} + Af_1 + Af_2 \quad (4)$$

$$E_{slab,1}^{substrate} = E_{bulk}^{substrate} + As_1 + As_2 \quad (5)$$

$$E_{slab,2}^{substrate} = 2E_{bulk}^{substrate} + As_1 + As_2 \quad (6)$$

$$E_{ht} = E_{bulk}^{substrate} + E_{bulk}^{film} + A\gamma + As_1 + Af_2 \quad (7)$$

$$E_{ch} = \frac{E_{ht} - (E_{slab,1}^{film} + E_{slab,1}^{substrate})}{A} = \gamma - (s_2 + f_1) \quad (8)$$

$$E_{it} = \frac{E_{ht} - \frac{1}{2} (E_{slab,2}^{film} + E_{slab,2}^{substrate})}{A} = \gamma - \left[\frac{1}{2} (s_2 - s_1) + \frac{1}{2} (f_1 - f_2) \right] \quad (9)$$

It can be seen from Eqs. (8) and (9) that both E_{ch} and E_{it} have residual errors if the slabs have asymmetric surface energies. However, our derivation and analysis in Supplementary Material S3 show that E_{it} represents a more accurate form than E_{ch} .

For the randomly sampled interfaces, we compared MLIP-predicted static values of E_{ht} , E_{it} , and E_{ch} with DFT-calculated values to evaluate the applicability of these MLIPs in modeling the PES of heterogeneous interfaces. Next, for each (i_m, i_t) , we performed Bayesian optimization using MLIP-calculated static E_{it} in the RBT space. The interface with the lowest predicted static energy was selected for full structural relaxation, yielding the optimized and relaxed $E_{it}(i_m, i_t)$ and the corresponding relaxed IBM structure $I(i_m, i_t)$. Each $I(i_m, i_t)$ was subsequently refined using DFT calculations. Following the approach in Ogric [32,34], we assessed the ranking consistency of $E_{it}(i_m, i_t)$ predicted by MLIP and DFT as a validity criterion for determining whether an MLIP reliably identifies the most stable interface structures.

2.5. Materials and DFT simulation

We applied our workflow to simulate three representative film|substrate interface systems relevant to advanced lithium batteries: (1) $\text{Li}_2\text{S}|\text{Ni}_3\text{S}_2$, a cathode interface in lithium-sulfur batteries, where an artificially deposited Ni_3S_2 film serves as a catalyst [51]; (2) $\text{LiF}|\text{Li}_3\text{MnCoNiO}_6$ (NCM), a CEI/cathode interface in NCM-based batteries [52–56]; and (3) $\text{Li}_3\text{PS}_4|\text{Li}$, an electrolyte/anode interface in lithium-metal batteries [57–60]. First-principles DFT calculations were performed using the Vienna Ab initio Simulation Package (VASP), with the projector augmented wave method [61,62]. The Perdew–Burke–Ernzerhof (PBE) generalized gradient approximation (GGA) was used to model exchange–correlation interactions, with the cutoff energy of the plane-wave basis set for the electron wavefunction to 520 eV. The energy convergence criterion for electronic self-consistent iteration was set to 10^{-5} eV. The structural relaxation was finished once the force on every atom was less than $0.05 \text{ eV } \text{\AA}^{-1}$. For the random sampling simulation which only calculates static energy, the vacuum thickness was set to 8 Å; and the slab thicknesses were set to be periodicity replicas reaching 12 Å. For interface ranking simulation which involves structural optimization, according to the convergence test in Figs. S4 and S5, the vacuum thickness was set to 10 Å; the slab thicknesses for $\text{Li}_2\text{S}|\text{Ni}_3\text{S}_2$ and $\text{LiF}|\text{NCM}$ were set to be periodicity replicas reaching 10 Å; for $\text{Li}_3\text{PS}_4|\text{Li}$ interfaces, this value was set to 15 Å. Brillouin zone sampling was performed with a fixed k -points density of 100 k -points \AA^{-3} . While including a vacuum region in supercell calculations can introduce energy artifacts, enabling dipole corrections in VASP can mitigate this issue. However, our benchmark calculations (Fig. S6) indicate that dipole corrections have a negligible impact on determining the ground-state interface and the relative stability. To avoid self-consistency convergence issues, we opted to disable dipole corrections in all calculations. Atomate [63] and FireWorks [64] workflows were implemented to automate VASP calculation for all the needed structures shown in Fig. 3. The workflows also support automate output analysis for calculating E_{it} and E_{ch} , as well as for MLIP benchmark assessment.

3. Results and discussion

3.1. Lattice matching and termination detecting

Here, we present the lattice matches and terminations determined for $\text{LiF}|\text{NCM}$ interfaces. We set the maximum matching area to 27 \AA^2 , and the maximum length and angle strain to 1%. The von Mises strain ε_v is applied to describe the interface strain for its importance in materials' elastic limitation (yield strength) [65]. A two-dimensional interface satisfies general plane stress condition in which ε_v is derived as

$$\varepsilon_v = \sqrt{\varepsilon_{11}^2 - \varepsilon_{11}\varepsilon_{22} + \varepsilon_{22}^2 + 3\varepsilon_{12}^2} \quad (10)$$

ε_{11} and ε_{22} are the two principal components in the interface plane, ε_{12} is the shear component. In this study, we apply strain solely to the film material, which is a simplified approach but reasonable for real cases when the desired simulation region is in the vicinity of the interface. A more comprehensive protocol should distribute the strain into the two crystals according to their Young's moduli and relative thicknesses, which is beyond the scope of this work but could be addressed in future implementation.

Fig. 4(a and b) depicts the stereographic projection of all matching lattice planes, categorized into three non-equivalent lattice matching types (denoted as type 0, 1, 2) using our equivalence analysis algorithm. This visualization effectively captures the anisotropy in lattice matching. LiF exhibits 68 matching planes uni-

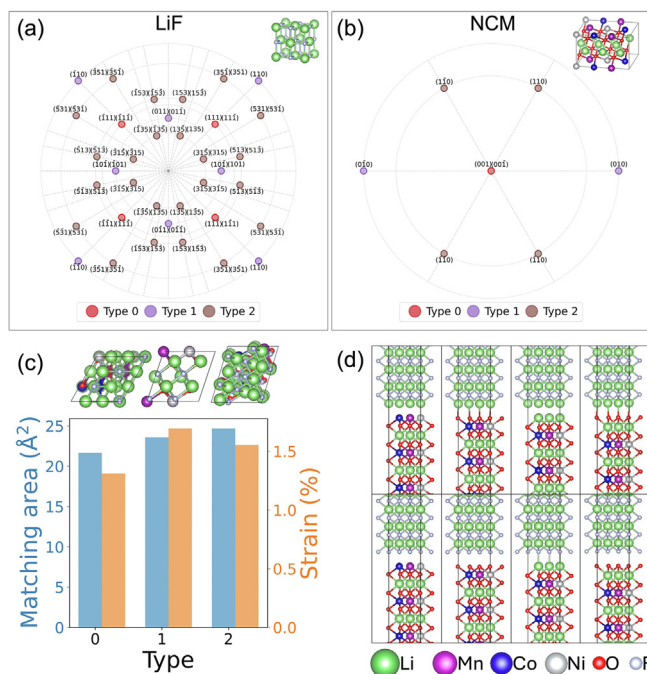


Fig. 4. Lattice matching and termination exploring results of the $\text{LiF}|\text{NCM}$ interfaces. (a, b) The found matching lattice planes sorted by equivalence. (c) Matching area and von Mises strain ε_v of the non-equivalent matching types. (d) Non-equivalent terminations belonging to matching type 1.

formly distributed across the stereographic projection, indicating a nearly isotropic nature. In contrast, NCM displays only eight matching planes, with maximum indices not exceeding 1, highlighting its pronounced anisotropy. These findings provide key insights into CEI structure analysis and design for NCM-based batteries. The formation of well-bonded interfaces with relatively small lattice mismatch between two crystalline materials depends not only on interface energy but also on the number of potential matching planes, which can be interpreted as an entropy-driven effect [66]. From this perspective, LiF demonstrates a strong capability to match NCM, aligning with the frequent observation of LiF -rich CEIs on NCM cathodes [52–56]. Moreover, the pronounced anisotropy of NCM suggests a potential strategy for enhancing passivation by selectively exposing its low-index surfaces.

Fig. 4(c) presents the matching area and strain (ε_v) for the three identified non-equivalent matching types, along with their atomic matching patterns viewed perpendicular to the interface plane. Three non-equivalent matches exhibit similar lattice matching properties; however, this does not necessarily imply comparable formation probabilities. By integrating lattice matching information with optimized interface energies, as will be discussed in later sections, one can intuitively assess the full spectrum of interface formation possibilities between any two crystals. This makes InterOptimus a powerful tool for both interpreting experimental results and exploring novel interface structures. Fig. 4(d) illustrates the eight non-equivalent terminations explored for lattice matching type 1, derived from combinations of two non-equivalent LiF atomic planes and four non-equivalent NCM atomic planes. RBT analysis will then be used to determine the relative position of two half-crystals that result in the ground state of the interface.

3.2. Validation of MLIPs

3.2.1. Random sampling

Fig. 5 illustrates the calculated static E_{ch} and E_{it} for interfaces generated through random sampling of RBT in $\text{Li}_2\text{S}|\text{Ni}_3\text{S}_2$, $\text{LiF}|\text{NCM}$

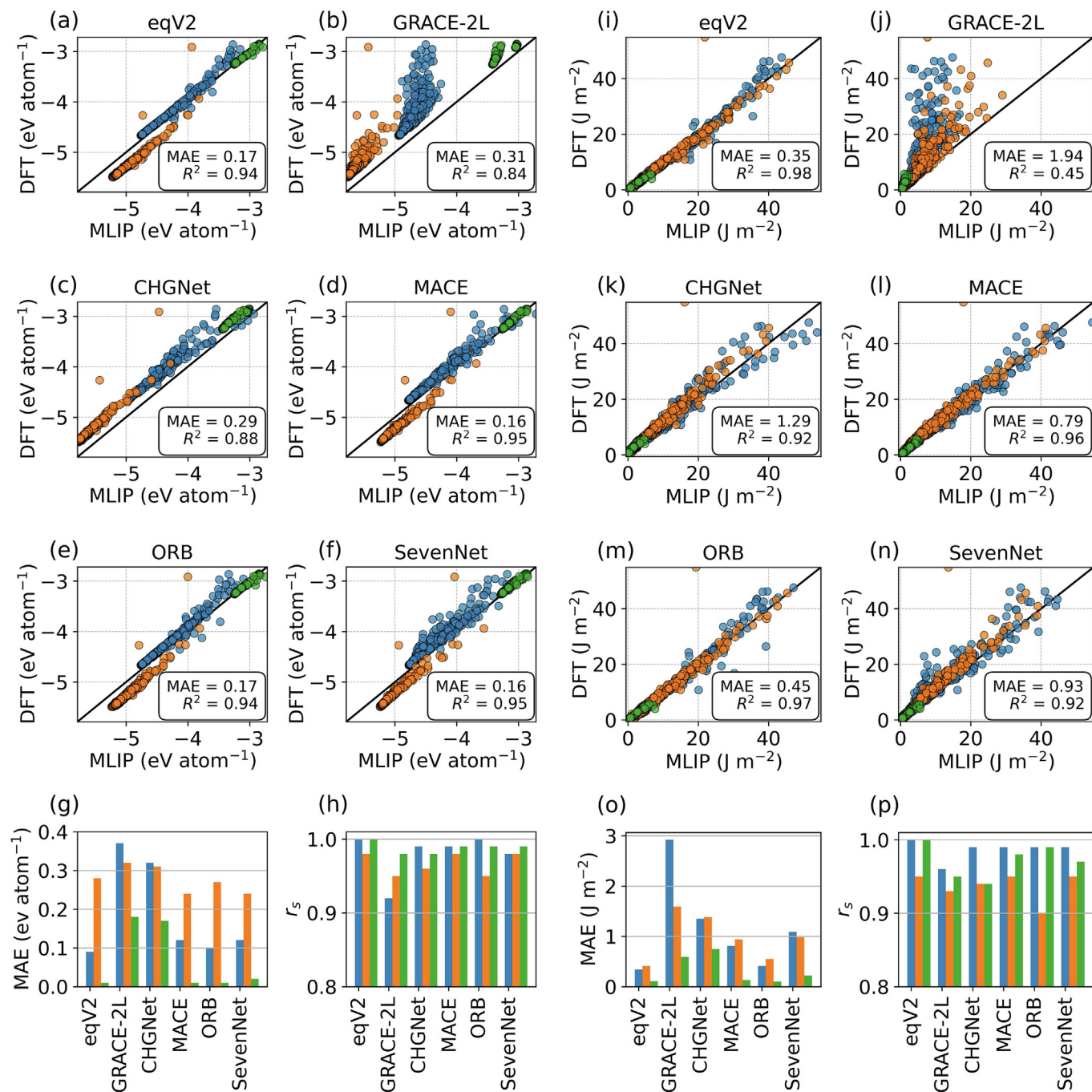


Fig. 5. Calculated static (a–h) E_{ht} and (i–p) E_{it} . (a–f, i–n) DFT- and MLIP-calculated values. (g, o) Prediction mean absolute error (MAE). (h, p) Spearman's rank correlation coefficient r_s . Blue, orange, and green represent interface systems of $\text{Li}_2\text{S}|\text{Ni}_3\text{S}_2$, $\text{LiF}|\text{NCM}$, and $\text{Li}_3\text{PS}_4|\text{Li}$.

NCM, and $\text{Li}_3\text{PS}_4|\text{Li}$ systems. E_{ch} result is quite similar to E_{it} and is illustrated in Fig. S7. As shown in Fig. 5(a–f), GRACE-2L exhibits significantly lower accuracy in the high-energy region across all systems compared to other MLIPs. CHGNet slightly underestimates E_{ht} , with an average error of around $0.30 \text{ eV atom}^{-1}$. In contrast, the other four MLIPs—eqV2, MACE, ORB, and SevenNet—demonstrate substantially better accuracy, though they all slightly overestimate E_{ht} for $\text{LiF}|\text{NCM}$. However, as shown in Fig. 5(i–n), these errors largely canceled out in the calculations of E_{it} , with the exception of GRACE-2L, which still significantly underestimates E_{it} at higher energy levels.

These findings highlight the predictive capability of leading universal MLIPs for interface systems in Li batteries. Among the three

investigated interface systems, the $\text{Li}_2\text{S}|\text{Ni}_3\text{S}_2$ interface, composed of sulfides with the same anions in both crystals, represents a relatively simple interface system. In contrast, the $\text{LiF}|\text{NCM}$ interface, consisting of oxide and fluoride compounds, presents a greater challenge for MLIP accuracy due to its higher chemical complexity that is unprecedented in their training process. Both systems are representative of heterogeneous structures at the cathode side. Meanwhile, the $\text{Li}_3\text{PS}_4|\text{Li}$ interface, composed of Li metal and a sulfide compound, represents a critical electrolyte/anode interface in solid-state lithium batteries employing Li metal anodes and sulfur-based electrolytes, a highly reactive system. According to the prediction errors for different interface systems shown in Fig. 5(g and o), except for GRACE-2L and CHGNET with relatively low accuracy,

cies, the absolute energy prediction errors for the three systems follows: $\text{LiF|NCM} > \text{Li}_2\text{S|Ni}_3\text{S}_2 > \text{Li}_3\text{PS}_4\text{|Li}$. $\text{Li}_3\text{PS}_4\text{|Li}$ exhibits an extremely high accuracy approaching to $0.01 \text{ eV atom}^{-1}$. Comparing the system complexities, LiF|NCM has a higher complexity in elemental types while $\text{Li}_3\text{PS}_4\text{|Li}$ is distinctive from its combination of ionic and metallic bonds. This result indicates that for universal MLIPs, promoting prediction accuracy for an interface involving two crystals with different chemical bond properties is not as difficult as for an interface with higher elemental composition complexity. This is also reflected by the Spearman's rank correlation coefficient values (r_s) shown in Fig. 5(p), presenting a notably inferior robustness in LiF|NCM . Particularly, ORB has a relatively low 0.9 value, despite its low MAE in E_{it} . However, as will be shown in next chapter, this r_s value is already sufficient to identify the ground-state interface. Overall, such resulting accuracy of these MLIPs across chemically diverse interfaces suggests their potential validity in capturing the PES of heterogeneous interfaces, despite that they were primarily trained on DFT data for isolated single-crystal structures.

3.2.2. Interface ranking

As discussed in Section 2.4, achieving efficient exhaustive screening to obtain the ground-state interface structure relies on accurately predicting the rank of the RBT-optimized and further relaxed effective interface energy $E_{it}(i_m, i_t)$ and identifying the corresponding interface structure $I(i_m, i_t)$ across all (i_m, i_t) groups. To determine suitable MLIPs for interface ranking, we evaluated the MLIPs' computational cost by relaxing a $\text{Li}_3\text{PS}_4\text{|Li}$ interface with 118 atoms using an Apple M3 Pro chip with 12 CPU cores. Table 1 presents the average time per relaxing step during the initial 100 steps, along with the MAE of E_{it} shown in Fig. 5(i–n).

Considering a balanced computational cost and accuracy, as shown in Table 1, we selected ORB and SevenNet for interface energy ranking benchmarks, exhibiting about 600–770 times of acceleration compared to DFT. Specifically, for each (i_m, i_t) group, 50 trials of Bayesian optimization were performed to find the interface with optimize RBT where the static E_{it} was calculated by MLIP. Then, the RBT-optimized interface and the slabs shown in Fig. 3 to calculate E_{it} were relaxed by MLIP. The MLIP-relaxed structures are subsequently relaxed by DFT.

Calculation of E_{it} using Eq. (9) involves calculation of slab energy with two surfaces exposed to vacuum. This imposes additional demands on the accuracy of MLIPs in modeling slab structures. Furthermore, significant surface reconstruction in slabs can notably distort the bulk region or even induce phase transitions (Fig. S8). Consequently, E_{it} computed via Eq. (9) becomes problematic due to the non-identical surface and bulk energies between isolated slabs and those in the IBM (as shown in Fig. 3). To circumvent these issues and focus on evaluating MLIP accuracy for interfaces with as few surface impacts as possible, we imposed structural optimization constraints during the calculation of E_{it} for different interfaces. All slabs depicted in Fig. 3 were set to remain static, being identical to their bulk structures. This constraint is to enforce the slabs to be as identical as possible to the regions in the IBM far away from the interface to make an ideal interface model between two perfect crystals. Following this, Bayesian optimization was employed to determine the RBT-optimized IBM. Subsequently, the outermost one or two atomic layers (not exceeding 5 Å) were fixed in the x -, y -, and z - dimensions during

the structural optimization process. As shown in Figs. S4 and S5, applying constraints slightly changes the calculated interface energy value because the RBT was not capable to be further relaxed. This would not be a significant issue because this error can be minimized by increasing the number of Bayesian optimization trials to enhance the accuracy of initial RBT positions and by utilizing MLIPs with higher precision. As will be presented subsequently, the energy difference caused by fixing RBT is negligible in most cases.

MLIP validity is reflected by both the energy and atomic coordinates prediction error compared to DFT results. For better presentation, for each (i_m, i_t) group, we denote two sets of computed interface effective energies $E_{it}(i_m, i_t)$ and interface structures $I(i_m, i_t)$ by MLIP and DFT respectively as $E_{it}^{\text{MLIP}}(i_m, i_t)$, $E_{it}^{\text{DFT}}(i_m, i_t)$ and $I^{\text{MLIP}}(i_m, i_t)$, $I^{\text{DFT}}(i_m, i_t)$. The prediction error and ranking robustness are reflected by the MAE and r_s resulted from using $E_{it}^{\text{MLIP}}(i_m, i_t)$ to predict $E_{it}^{\text{DFT}}(i_m, i_t)$, as well as the average atomic displacement ΔX from $I^{\text{MLIP}}(i_m, i_t)$ relaxed into $I^{\text{DFT}}(i_m, i_t)$. Fig. 6 illustrates the ranking results of these defined values. A few DFT-non-converged results were eliminated and not shown here. As all the non-converged interfaces' $E_{it}^{\text{MLIP}}(i_m, i_t)$ values are higher than 50% of the interfaces in the same group and the number of them is quite small, eliminating them will not significantly affect ground-state interface determination and the evaluation of the overall ranking robustness. This also reflects that $E_{it}^{\text{MLIP}}(i_m, i_t)$ values can be used to eliminate high-energy interfaces which are difficult to converge in DFT simulation.

According to Fig. 6, both ORB and SevenNet successfully identified the lowest-energy interfaces from the sampled structures, though for $\text{Li}_2\text{S|Ni}_3\text{S}_2$ and $\text{Li}_3\text{PS}_4\text{|Li}$ systems they identified different ground-state interfaces. ORB identified (1,0) and (0,3) as the ground states in $\text{Li}_2\text{S|Ni}_3\text{S}_2$ and $\text{Li}_3\text{PS}_4\text{|Li}$ while SevenNet identified (0,2) and (0,1). For the $\text{Li}_2\text{S|Ni}_3\text{S}_2$ system, the ORB- and SevenNet-explored $I^{\text{DFT}}(1, 0)$ and $I^{\text{DFT}}(0, 2)$ structures have different E_{it}^{DFT} while their interface structures are almost identical, as shown in Fig. S9(a–d). As explained above, this energy disparity derives from the difference in their optimized RBT points which were fixed during the following structure relaxation. As seen, such difference due to RBT is negligible compared with the energy difference between them and other $I(i_m, i_t)$ structures. Further relaxation by canceling the constraint of the outermost atoms on the film surface can eliminate this difference. However, as discussed before, cancelling the constraint might cause severe structural instability or phase transition in the IBM or slab models. Therefore, for interfaces with close E_{it} values explored by this constraint-applied sampling method, identifying their relative stability requires additional techniques such as surface passivation, and more comprehensive investigation on the relationship between E_{it} and γ . These will be included in our future research. For current studies, IBMs with closely low E_{it} values can both be investigated because they could both have high probabilities to exist. The $\text{Li}_3\text{PS}_4\text{|Li}$ system is highly reactive and exhibits notably negative E_{it} values. For such a reactive system, it might be problematic to use the term 'ground-state interface' because with sufficient dynamic energy, they could react into a totally new reaction product, which should be more stable than the interface. Therefore, the interfaces simulated here should be considered as the intermediate products which can perform many

Table 1
Computational cost and accuracy of MLIPs and DFT to relax an interface.

MLIP	eqV2	GRACE-2L	CHGNet	MACE	ORB	SevenNet	DFT
Cost/step (s)	14.18	0.49	0.23	0.8	0.37	0.29	223.11
E_{it} MAE (J m^{-2})	0.35	1.94	1.29	0.79	0.45	0.93	\

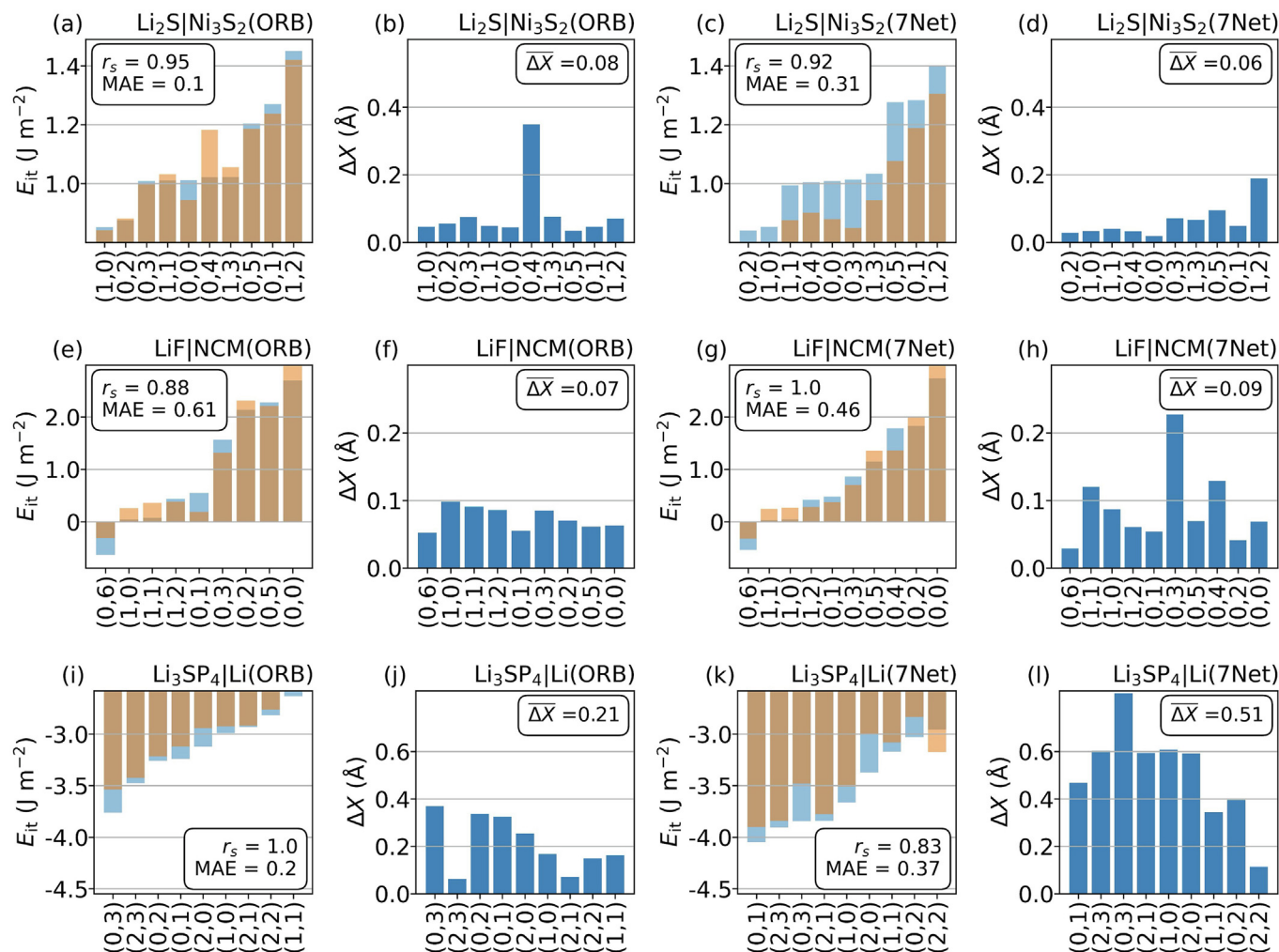


Fig. 6. Interface ranking results. $E_{it}^{\text{MLIP}}(i_m, i_t)$ (orange bar) and $E_{it}^{\text{DFT}}(i_m, i_t)$ (blue bar) for (a, c) $\text{Li}_2\text{S}|\text{Ni}_3\text{S}_2$, (e, g) $\text{LiF}|\text{NCM}$, and (i, k) $\text{Li}_3\text{PS}_4|\text{Li}$. ΔX for (b, d) $\text{Li}_2\text{S}|\text{Ni}_3\text{S}_2$, (f, h) $\text{LiF}|\text{NCM}$, and (j, l) $\text{Li}_3\text{PS}_4|\text{Li}$.

different states. These states can be regarded as different reaction routines or at different reaction extents. Such reactive IBMs are of importance because they can be applied to investigate the atomic structure at the position nearest the reaction interface. ORB and SevenNet explored severely disparate $I^{\text{DFT}}(0, 3)$ and $I^{\text{DFT}}(0, 1)$ structures as shown in Fig. S9(e–h). It can be seen that interfaces sampled by SevenNet react deeper at 0 K thus presenting notably lower E_{it} . Despite such disparity, both ORB and SevenNet performed high ranking consistency and E_{it} accuracy for $\text{Li}_3\text{PS}_4|\text{Li}$. For $\text{LiF}|\text{NCM}$ system, both ORB and SevenNet successfully identified the ground-state (0,6), the only IBM with a negative E_{it} value. This might suggest that these two crystals can perform orientation-preferred chemical reaction. According to Figs. S10 and S11(d), the negative E_{it} value indicates that the Li-F layer at interface is further stabilized when it sits between another Li-F layer in the LiF and the transition-metal-O layer in the NCM. For $\text{Li}_2\text{S}|\text{Ni}_3\text{S}_2$ and $\text{LiF}|\text{NCM}$ systems, almost $I^{\text{MLIP}}(i_m, i_t)$ structures are very close to $I^{\text{DFT}}(i_m, i_t)$ structures with small ΔX values. According to Figs. S10(a–d) and S11(a–d), they are nearly indistinguishable to the naked eye. For the $\text{Li}_3\text{PS}_4|\text{Li}$ interfaces, although they have notably higher ΔX values, according to Figs. S10(e, f) and S11(e, f), the $I^{\text{MLIP}}(i_m, i_t)$ and $I^{\text{DFT}}(i_m, i_t)$ interfaces are still quite similar with most atoms having close coordinates. These results indicate that using MLIPs is not only capable to determine the ground-

state interface, but also provides a good initial structure close to the DFT-simulated stable state. This can further significantly reduce time cost because an unstable complex interface structure might need many ionic steps to converge. Overall, the ranking results verified the capability of the two selected MLIPs in determining the ground-state interfaces in all the three systems. According to the MAE, r_s , and ΔX values shown in Fig. 6, ORB performs slightly better than SevenNet.

According to the ranking results, MLIPs can be applied to dramatically promote the efficiency. For each simulated interface system, both ORB and SevenNet accurately identified and ranked the interfaces with the lowest and second-lowest effective interface energies, in agreement with DFT results. Using these MLIPs, InterOptimus can efficiently find the ground-state interface by performing only one or two DFT relaxations for $I^{\text{MLIP}}(i_m, i_t)$ structures with lowest $E_{it}^{\text{MLIP}}(i_m, i_t)$ values. This offers a very significant efficiency promotion. In practical applications, one can apply a conservative strategy by appropriately including more low-energy interfaces (e.g. the lowest-five interfaces) in DFT simulation. Generally, a > 90% efficiency promotion could be achieved.

These results show that, unlike previous tools that rely on optimized classical atomic potentials [32,34] or MLIPs trained solely on specific material systems [67], universal MLIPs offer greater robustness and transferability, making them applicable to a wider

range of material modeling problems. Furthermore, compared with classical atomic potentials, the accuracy of MLIPs can be less difficult to be improved through a fine-tuning process using a moderate number of randomly sampled interface structures.

3.3. Future applications in batteries

Battery performance is widely recognized to be heavily influenced by the properties of the interphase [11]. This influence can be controlled either by optimizing the in-situ formation process of the interphase through electrolyte design or by employing artificial protective films. However, the complexity and ongoing debate regarding the precise correlation between interphase properties and battery performance suggest that a universally effective strategy remains exclusive. For instance, Wan et al. [11] have recently suggested that both CEI and SEI should exhibit weak bonding to the electrodes, thereby maintaining a high interface energy. This, in turn, would minimize stress and damage to the interphase during the charging or discharging process, even when the cathode and anode crack. This viewpoint is particularly relevant for SEI design in Li-metal batteries, where the inorganic compounds commonly observed in SEI, including LiF, Li₂O, and Li₂CO₃, are generally lithiophobic [68,69]. Conversely, many high-capacity cathodes, such as NCM, share strong chemical bonding characteristics with these interfacial compounds, which allows for the formation of stable, well-bonded interfaces under suitable lattice matching and termination conditions. For example, our calculations of LiF|NCM interfaces show that the most stable configuration exhibits a negative effective interface energy. Moreover, for other advanced battery systems, such as those utilizing Li-rich Mn-based cathodes, the primary degradation mechanism is associated with the cathode fracture due to large volume changes and Jahn-Teller distortions, rather than interphase instability. In these cases, emerging strategies are focusing on designing an artificial protective CEI that forms a robust, well-bonded interface with the cathode, thereby mitigating cathode fracture [70,71]. These findings challenge the perspective put forth by Wan et al., highlighting the need for a flexible, system-specific approach to interphase design, which considers the dominant degradation mechanisms and tailors the interphase properties accordingly.

Improving interphase properties in batteries necessitates a more nuanced understanding of how various components contribute to interfacial degradation, especially their interactions with the electrodes and electrolytes. Recent advances in atomic-level and in-situ characterization techniques have shown significant potential for revealing the ion transport and mechanical properties of interphases [72–74]. Integrating these advanced techniques with explicit atomic models enabled by InterOptimus can provide a deeper understanding of the fundamental mechanisms that governs the correlation between interphase characteristics and battery performance. This integration will be instrumental in guiding the development of next-generation battery design strategies. Several potential applications of this workflow include:

- (1) *Investigating Li⁺ transport across heterogeneous interfaces.* A promising avenue of research lies in exploring the Li⁺ transport properties across and through heterogeneous interfaces composed of different inorganic compounds within the interphase. While fluorination has often been viewed as beneficial for stabilizing the interphase, some studies suggest that interphases dominated by oxides and carbonates also exhibit promising battery performance. These studies indicate that the fluorine distribution in such interphases may be too sparse to significantly enhance performance [72,73,75]. Additionally, artificially deposited LiF SEIs have been found to exhibit excessive resistance, failing to deliver

the same performance as in situ-deposited LiF coexisting with other inorganic compounds [76]. These observations imply that high interfacial Li⁺ kinetics could stem from the heterogeneity of the interphase rather than from one single interfacial component. This hypothesis, to the best of our knowledge, remains underexplored and presents an opportunity for systematic investigation.

- (2) *High-throughput screening for novel artificial interphases.* The design of protective CEIs for Li-rich Mn-based cathodes offers another promising application. Such a CEI must possess a range of properties, such as electrochemical stability against both the high-voltage cathode and electrolyte, high Li⁺ conductivity with low electronic conductivity, and thermodynamic stability for synthesis. In addition to these bulk properties, favorable interfacial characteristics are essential for optimal compatibility. High-quality crystal materials databases [27] can serve as an initial screening tool to identify candidate materials based on their bulk properties. Subsequently, InterOptimus can refine this selection by evaluating materials for lattice matching to the cathode, low interface energy, a suitable interface band structure [77,78], and high Li⁺ conductivity at the interface. This methodology could also be applied to investigate coating materials for the protection of electrolyte against reductive Li metal anode [79].
- (3) *Data-driven research for interfaces in batteries.* While the efficiency of MLIPs in predicting ground-state interface structures has been illustrated in this work, calculating battery performance metrics, such as Li⁺ conductivity, can still be computationally expensive due to the need for enormous simulation time steps and numerous DFT calculations to fine tune MLIPs. Data-driven methods are becoming promising in exploring new battery materials including alloys for metal-based anode [80], organic electrolytes [81], and inorganic crystalline electrolytes [29]. Recent advances in generative models offer a promising alternative, enabling the direct generation of structures with desired properties without the need for expensive property calculations [29]. Given that InterOptimus significantly enhances the efficiency of interface simulations through robust symmetry analysis and the use of universal MLIPs, it is poised to contribute to the development of high-quality interface calculation datasets. These datasets can, in turn, be used to train generative models, further accelerating the discovery and optimization of high-performance interfaces. For example, leveraging pre-computed interface structures with high stability, one can train a generative adversarial network (GAN) to predict the formation likelihood of stable interfaces between two arbitrary crystals without requiring additional calculations. Furthermore, the identified IBMs with optimal interface properties such as interface-ion-conductivities can be utilized to train diffusion models through the methodology described in ref. [29]. By implementing appropriate constraints on the bulk regions to enforce ideal interface configurations, this approach facilitates the generation of novel IBMs with enhanced properties.

4. Conclusions

We present InterOptimus, an integrated workflow designed to facilitate screening ground-state heterogeneous interfaces between two arbitrary crystals, exemplified by key interfaces in lithium batteries. Compared to previous tools, InterOptimus introduces several key innovations. First, it offers enhanced visualization of lattice matching results using stereographic projection, which aligns with crystallographic conventions and is more widely

accepted. Additionally, we have implemented advanced symmetry analysis algorithms to identify non-equivalent lattice matches and lattice plane terminations in a bicrystal context, offering a more robust approach than simply considering the symmetry of isolated single crystals. Moreover, our approach integrates state-of-the-art universal MLIPs, enabling accelerated calculation and optimization of interface structure energies. We evaluate the accuracy of these MLIPs on three representative interface material pairs in lithium batteries, $\text{Li}_2\text{S}/\text{Ni}_3\text{S}_2$, LiF/NCM , and $\text{Li}_3\text{PS}_4/\text{Li}$. Our benchmarks show that they achieve accuracy comparable to DFT method in modeling the PES of interfaces, with interface energy prediction error within 0.30 J m^{-2} and with ranking robustness reflected by Spearman's rank correlation coefficient reaching 0.90. By leveraging these MLIPs, InterOptimus allows for precise ranking of interface energies across different lattice matches and terminations, helping to identify the ground-state interface structures through an efficient screening process requiring only a single DFT relaxation, enhancing the efficiency by over 90%. Future applications of the workflow will support the investigation of structure-property relationships in important interfacial structures and accelerate interface design research for next-generation high performance lithium battery materials.

CRedit authorship contribution statement

Yaoshu Xie: Writing – review & editing, Writing – original draft, Visualization, Validation, Software, Project administration, Methodology, Investigation, Formal analysis, Data curation, Conceptualization. **Jun Yang:** Writing – review & editing, Validation, Software, Methodology, Investigation, Formal analysis, Data curation, Conceptualization. **Yun Cao:** Writing – review & editing, Validation, Software, Methodology, Investigation, Formal analysis, Data curation, Conceptualization. **Wei Lv:** Writing – review & editing, Supervision, Resources, Project administration, Investigation, Conceptualization. **Yan-Bing He:** Writing – review & editing, Validation, Supervision, Software, Resources, Project administration, Methodology, Investigation, Funding acquisition, Formal analysis, Data curation, Conceptualization. **Lu Jiang:** Writing – review & editing, Validation, Supervision, Software, Resources, Project administration, Methodology, Investigation, Formal analysis, Data curation, Conceptualization. **Tingzheng Hou:** Writing – review & editing, Validation, Supervision, Software, Resources, Project administration, Methodology, Investigation, Funding acquisition, Formal analysis, Data curation, Conceptualization.

Declaration of competing interest

The authors declare that they have no known competing financial interests or personal relationships that could have appeared to influence the work reported in this paper.

Acknowledgments

This work was supported by the National Natural Science Foundation of China (92470110), the Special Funds for the Development of Strategic Emerging Industries in Shenzhen (XMHT20240108008), and the Shenzhen Stable Support Program for Higher Education Institutions (WDZC20231126215806001).

Code availability

Our package is now publicly available at: <https://github.com/HouGroup/InterOptimus>.

Appendix A. Supplementary material

Supplementary data to this article can be found online at <https://doi.org/10.1016/j.jechem.2025.03.007>.

References

- [1] Q. Liu, Y. Sun, S. Wang, Q. An, L. Duan, G. Zhao, C. Wang, K. Doyle-Davis, H. Guo, X. Sun, *Mater. Today* 64 (2023) 21–30.
- [2] O.B. Chae, B.L. Lucht, *Adv. Energy Mater.* 13 (2023) 2203791.
- [3] Y. Xiao, Y. Wang, S.-H. Bo, J.C. Kim, L.J. Miara, G. Ceder, *Nat. Rev. Mater.* 5 (2020) 105–126.
- [4] R. Xiong, H. Li, B.-A. Mei, H. He, W. Shen, *J. Energy Chem.* 102 (2025) 734–744.
- [5] H. Zhang, D. Xu, F. Yang, J. Xie, Q. Liu, D.-J. Liu, M. Zhang, X. Lu, Y.S. Meng, *Joule* 7 (2023) 971–985.
- [6] J.R. Szczech, S. Jin, *Energy Environ. Sci.* 4 (2011) 56–72.
- [7] L. Sun, Y. Liu, R. Shao, J. Wu, R. Jiang, Z. Jin, *Energy Storage Mater.* 46 (2022) 482–502.
- [8] W. Xu, J. Wang, F. Ding, X. Chen, E. Nasybulin, Y. Zhang, J.-G. Zhang, *Energy Environ. Sci.* 7 (2014) 513–537.
- [9] H. Yuan, X. Ding, T. Liu, J. Nai, Y. Wang, Y. Liu, C. Liu, X. Tao, *Mater. Today* 53 (2022) 173–196.
- [10] R. Wang, W. Cui, F. Chu, F. Wu, *J. Energy Chem.* 48 (2020) 145–159.
- [11] H. Wan, J. Xu, C. Wang, *Nat. Rev. Chem.* 8 (2024) 30–44.
- [12] H. Chen, J. Wu, M. Li, J. Zhao, Z. Li, M. Wang, X. Li, C. Li, X. Chen, X. Li, Y.-W. Mai, Y. Chen, *eScience* 5 (2025) 100281.
- [13] Y. Qian, P. Niehoff, M. Börner, M. Grützeke, X. Mönnighoff, P. Behrends, S. Nowak, M. Winter, F.M. Schappacher, *J. Power Sources* 329 (2016) 31–40.
- [14] A. Wang, S. Kadam, H. Li, S. Shi, Y. Qi, *npj Comput. Mater.* 4 (2018) 15.
- [15] E. Peled, S. Menkin, *J. Electrochem. Soc.* 164 (2017) A1703.
- [16] P. Xu, X. Guo, B. Jiao, J. Chen, M. Zhang, H. Liu, X. Yu, M. Appleberry, Z. Yang, H. Gao, F. Yang, X. Weng, Y. Shen, J. Gu, Y.S. Meng, C. Brooks, S.P. Ong, Z. Chen, *Nat. Commun.* 15 (2024) 9842.
- [17] T. Binninger, A. Marcolongo, M. Mottet, V. Weber, T. Laino, *J. Mater. Chem. A* 8 (2020) 1347–1359.
- [18] Z. Yu, S.-L. Shang, J.-H. Seo, D. Wang, X. Luo, Q. Huang, S. Chen, J. Lu, X. Li, Z.-K. Liu, D. Wang, *Adv. Mater.* 29 (2017) 1605561.
- [19] K. Meier, T. Laino, A. Curioni, *J. Phys. Chem. C* 118 (2014) 6668–6679.
- [20] T. Lee, J. Qi, C.A. Gadre, H. Huyen, S.-T. Ko, Y. Zuo, C. Du, J. Li, T. Aoki, R. Wu, J. Luo, S.P. Ong, X. Pan, *Nat. Commun.* 14 (2023) 1940.
- [21] T. Hwang, P. Conlin, M. Cho, K. Cho, *J. Phys. Chem. C* 127 (2023) 7528–7535.
- [22] H.-K. Tian, B. Xu, Y. Qi, *J. Power Sources* 392 (2018) 79–86.
- [23] W. Fitzhugh, X. Chen, Y. Wang, L. Ye, X. Li, *Energy Environ. Sci.* 14 (2021) 4574–4583.
- [24] B.D. Lee, D.S. Gaval, H. Kim, S. Kim, M.Y. Cho, K. Pyo, Y.-K. Lee, W.B. Park, K.-S. Sohn, *J. Mater. Chem. A* (2025). <https://doi.org/10.1039/D4TA06927G>.
- [25] Z. Zheng, J. Zhou, Y. Zhu, *Chem. Soc. Rev.* 53 (2024) 3134–3166.
- [26] H. Guo, Q. Wang, A. Stuke, A. Urban, N. Artrith, *Front. Energy Res.* 9 (2021) 695902.
- [27] A. Jain, S.P. Ong, G. Hautier, W. Chen, W.D. Richards, S. Dacek, S. Cholia, D. Gunter, D. Skinner, G. Ceder, K.A. Persson, *APL Mater.* 1 (2013) 011002.
- [28] M. Hellenbrandt, *Crystallogr. Rev.* 10 (2004) 17–22.
- [29] C. Zeni, R. Pinsler, D. Zügner, A. Fowler, M. Horton, X. Fu, Z. Wang, A. Shysheya, J. Crabbé, S. Ueda, R. Sordillo, L. Sun, J. Smith, B. Nguyen, H. Schulz, S. Lewis, C.-W. Huang, Z. Lu, Y. Zhou, H. Yang, H. Hao, J. Li, C. Yang, W. Li, R. Tomioka, T. Xie, *Nature* 639 (2025) 624–632.
- [30] R.C. Pond, W. Bollmann, *Philos. Trans. R. Soc. London. Ser. A, Math. Phys. Sci.* 292 (1979) 449–472.
- [31] R.C. Pond, D.S. Vlachavas, *Proc. R. Soc. London. A. Math. Phys. Sci.* 386 (1983) 95–143.
- [32] S. Moayedpour, D. Dardzinski, S. Yang, A. Hwang, N. Marom, *J. Chem. Phys.* 155 (2021) 034111.
- [33] S.P. Ong, W.D. Richards, A. Jain, G. Hautier, M. Kocher, S. Cholia, D. Gunter, V.L. Chevrier, K.A. Persson, G. Ceder, *Comput. Mater. Sci.* 68 (2013) 314–319.
- [34] S. Toso, D. Dardzinski, L. Manna, N. Marom, *ACS Nano* 19 (2025) 5326–5341.
- [35] M. Neumann, J. Gin, B. Rhodes, S. Bennett, Z. Li, H. Choubisa, A. Hussey, J. Godwin, *arXiv preprint arXiv:2410.22570* (2024).
- [36] A. Zur, T.C. McGill, *J. Appl. Phys.* 55 (1984) 378–386.
- [37] H. Zheng, X.-G. Li, R. Tran, C. Chen, M. Horton, D. Winston, K.A. Persson, S.P. Ong, *Acta Mater.* 186 (2020) 40–49.
- [38] S. Kiyohara, H. Oda, K. Tsuda, T. Mizoguchi, *Jpn. J. Appl. Phys.* 55 (2016) 045502.
- [39] R.C. Pond, V. Vitek, P.B. Hirsch, *Proc. R. Soc. London. A. Math. Phys. Sci.* 357 (1977) 453–470.
- [40] R.C. Pond, P.B. Hirsch, *Proc. R. Soc. London. A. Math. Phys. Sci.* 357 (1977) 471–483.
- [41] Y. Xie, K. Shibata, T. Mizoguchi, *arXiv preprint arXiv:2211.15173* (2022).
- [42] D.A. Smith, R.C. Pond, *Int. Metals Rev.* 21 (1976) 61–74.
- [43] H. Grimmer, W. Bollmann, D.H. Warrington, *Acta Crystallogr. A* 30 (1974) 197–207.
- [44] Y. Xie, K. Shibata, T. Mizoguchi, *Comput. Phys. Commun.* 273 (2022) 108260.
- [45] B. Deng, P. Zhong, K. Jun, J. Riebesell, K. Han, C.J. Bartel, G. Ceder, *Nat. Mach. Intell.* 5 (2023) 1031–1041.

- [46] L. Barroso-Luque, M. Shuaibi, X. Fu, B.M. Wood, M. Dzamba, M. Gao, A. Rizvi, C. L. Zitnick, Z.W. Ulissi, arXiv preprint arXiv:2410.12771 (2024).
- [47] Y. Park, J. Kim, S. Hwang, S. Han, J. Chem. Theory Comput. 20 (2024) 4857–4868.
- [48] A. Bochkarev, Y. Lysogorskiy, R. Drautz, Phys. Rev. X 14 (2024) 021036.
- [49] I. Batatia, P. Benner, Y. Chiang, A. M. Elena, D. P. Kovács, J. Riebesell, X. R. Advincula, M. Asta, M. Avaylon, W. J. Baldwin, F. Berger, N. Bernstein, A. Bhowmik, S. M. Blau, V. Čárář, J. P. Darby, S. De, F. Della Pia, V. L. Deringer, R. Elijošius, Z. El-Machachi, F. Falcioni, E. Fako, A. C. Ferrari, A. Genreith-Schriever, J. George, R. E. A. Goodall, C. P. Grey, P. Grigorev, S. Han, W. Handley, H. H. Heenen, K. Hermansson, C. Holm, J. Jaafar, S. Hofmann, K. S. Jakob, H. Jung, V. Kapil, A. D. Kaplan, N. Karimitari, J. R. Kermode, N. Kroupa, J. Kullgren, M. C. Kuner, D. Kuryla, G. Liepuoniute, J. T. Margraf, I.-B. Magdău, A. Michaelides, J. H. Moore, A. A. Naik, S. P. Niblett, S. Walton Norwood, N. O'Neill, C. Ortner, K. A. Persson, K. Reuter, A. S. Rosen, L. L. Schaaf, C. Schran, B. X. Shi, E. Sivonxay, T. K. Stenczel, V. Svahn, C. Sutton, T. D. Swinburne, J. Tilly, C. van der Oord, E. Varga-Umbrich, T. Vegge, M. Vondrák, Y. Wang, W. C. Witt, F. Zills, G. Csányi, arXiv preprint arXiv:2401.00096 (2023).
- [50] T. Frolov, W. Setyawan, R.J. Kurtz, J. Marian, A.R. Oganov, R.E. Rudd, Q. Zhu, Nanoscale 10 (2018) 8253–8268.
- [51] Z. Li, S. Zhang, J. Zhang, M. Xu, R. Tatara, K. Dokko, M. Watanabe, ACS Appl. Mater. Interfaces 9 (2017) 38477–38485.
- [52] S.Y. Kim, T. Yim, J. Energy Storage 99 (2024) 113264.
- [53] Y. Liao, N. Wang, X. Dai, W. Zhou, F. Wu, J. Wang, H. Chen, Y. Mai, Appl. Surf. Sci. 672 (2024) 160791.
- [54] K. Wei, J. Li, W. Huang, L. Wang, Solid State Ion. 405 (2024) 116436.
- [55] J. Li, Y. Zhang, X. Chen, L. Lu, H. Liu, F. Gao, S. An, X. Wang, X. Qiu, J. Electrochem. Soc. 171 (2024) 050528.
- [56] X. Cao, X. Ren, L. Zou, M.H. Engelhard, W. Huang, H. Wang, B.E. Matthews, H. Lee, C. Niu, B.W. Arey, Y. Cui, C. Wang, J. Xiao, J. Liu, W. Xu, J.-G. Zhang, Nat. Energy 4 (2019) 796–805.
- [57] N.D. Lepley, N.A.W. Holzwarth, Phys. Rev. B 92 (2015) 214201.
- [58] N.D. Lepley, N.A.W. Holzwarth, Y.A. Du, Phys. Rev. B 88 (2013) 104103.
- [59] J. Park, T. Watanabe, K. Yamamoto, T. Uchiyama, T. Takami, A. Sakuda, A. Hayashi, M. Tatsumisago, Y. Uchimoto, Chem. Commun. 59 (2023) 7799–7802.
- [60] N.L. Marana, S. Casassa, M.F. Sgroi, L. Maschio, F. Silveri, M. D'Amore, A.M. Ferrari, Langmuir 39 (2023) 18797–18806.
- [61] G. Kresse, J. Furthmüller, Phys. Rev. B 54 (1996) 11169–11186.
- [62] G. Kresse, D. Joubert, Phys. Rev. B 59 (1999) 1758–1775.
- [63] K. Mathew, J.H. Montoya, A. Faghaninia, S. Dwarakanath, M. Aykol, H. Tang, I.-H. Chu, T. Smidt, B. Bocklund, M. Horton, J. Dagdelen, B. Wood, Z.-K. Liu, J. Neaton, S.P. Ong, K. Persson, A. Jain, Comput. Mater. Sci. 139 (2017) 140–152.
- [64] A. Jain, S.P. Ong, W. Chen, B. Medasani, X. Qu, M. Kocher, M. Brafman, G. Petretto, G.-M. Rignanese, G. Hautier, D. Gunter, K.A. Persson, Concurrency Comput. Pract. Exper. 27 (2015) 5037–5059.
- [65] L.A. Zepeda-Ruiz, D. Maroudas, W.H. Weinberg, J. Appl. Phys. 85 (1999) 3677–3695.
- [66] J. Han, V. Vitek, D.J. Srolovitz, Acta Mater. 104 (2016) 259–273.
- [67] S. Moayedpour, I. Bier, W. Wen, D. Dardzinski, O. Isayev, N. Marom, J. Phys. Chem. C 127 (2023) 10398–10410.
- [68] X. He, X. Ji, B. Zhang, N.D. Rodrigo, S. Hou, K. Gaskell, T. Deng, H. Wan, S. Liu, J. Xu, B. Nan, B.L. Lucht, C. Wang, ACS Energy Lett. 7 (2022) 131–139.
- [69] B. Chen, J. Zhang, T. Zhang, R. Wang, J. Zheng, C. Liu, X. Liu, ACS Energy Lett. 8 (2023) 2221–2231.
- [70] M. Xu, M. Yang, M. Chen, L. Gu, L. Luo, S. Chen, J. Chen, B. Liu, X. Han, J. Energy Chem. 76 (2023) 266–276.
- [71] M. Xu, B. Sheng, Y. Cheng, J. Lu, M. Chen, P. Wang, B. Liu, J. Chen, X. Han, M.-S. Wang, S. Shi, Nano Res. 17 (2024) 4192–4202.
- [72] Y. Li, Y. Li, A. Pei, K. Yan, Y. Sun, C.-L. Wu, L.-M. Joubert, R. Chin, A.L. Koh, Y. Yu, J. Perrino, B. Butz, S. Chu, Y. Cui, Science 358 (2017) 506–510.
- [73] Y. Li, W. Huang, Y. Li, A. Pei, D.T. Boyle, Y. Cui, Joule 2 (2018) 2167–2177.
- [74] D. Cheng, J. Hong, D. Lee, S.-Y. Lee, H. Zheng, Chem. Rev. 125 (2025) 1840–1896.
- [75] W. Huang, H. Wang, D.T. Boyle, Y. Li, Y. Cui, ACS Energy Lett. 5 (2020) 1128–1135.
- [76] M. He, R. Guo, G.M. Hobold, H. Gao, B.M. Gallant, Proc. Natl. Acad. Sci. 117 (2020) 73–79.
- [77] M. Kohyama, R. Yamamoto, Phys. Rev. B 50 (1994) 8502–8522.
- [78] Y. Xie, K. Shibata, T. Mizoguchi, Acta Mater. 250 (2023) 118827.
- [79] J. Ke, G. Xu, F. Liu, C. Wang, J. Zhao, M. Wu, A. Zulfiqar, J. Wang, X. Sun, Adv. Funct. Mater. (2025). <https://doi.org/10.1002/adfm.202420170>.
- [80] X. Shi, L. Zhou, Y. Huang, C. Wu, Y. Wu, J. Li, Z. Hong, J. Energy Chem. 104 (2025) 62–68.
- [81] X. Yuan, X. Chen, Y. Zhou, Z. Yu, X. Kong, J. Energy Chem. 102 (2025) 52–62.